Supplementary Information of

Giant chlorine isotope effect of ion-molecule reaction

Yaya Zhi[1,†], Jie Hu[2,†], Jingchen Xie[1], Chun-Xiao Wu[2], Shan Xi Tian[1,2,3,4,*]

[1] *Department of Chemical Physics, Collaborative Innovation Center of Chemistry for Energy Materials (iChEM),University of Science and Technology of China, Hefei, 230026, China*

[2]*Hefei National Research Center for Physical Sciences at the Microscale, University of Science and Technology of China, Hefei, 230026, China*

[3] *Hefei National Laboratory, University of Science and Technology of China, Hefei, 230088, China*

[4]*State Key Laboratory of Molecular Reaction Dynamics, Dalian Institute of Chemical Physics, Chinese Academy of Sciences, Dalian, 116023, China*

† Contributed equally. *Corresponding author. Email: sxtian@ustc.edu.cn.

Table of Contents

1 Derivation of Eq. (2)

According to the terminological definitions (see ref. 7 and references cited therein), we have

Table S1 Parameters for Evaluating Cl-Isotope Effect

i	*1*	*2*	*3*
	$C_2H_2{}^{35}Cl_2$	$C_2H_2{}^{35}Cl{}^{37}Cl$	$C_2H_2{}^{37}Cl_2$
$n^{37}{}_{Cl,i}$	0	1	2
$P_i{}^a$	$(1-\Pi_R)^2=0.5741$	$2*\Pi_R*(1-\Pi_R)=0.3672$	$\Pi_R{}^2=0.0587$
$\theta^{35}{}_i$	1	$\frac{k_{35}}{k_{35}+k_{37}}$	0
$\theta^{37}{}_i$	0	$\frac{k_{37}}{k_{35}+k_{37}}$	1
$^{35}Cl_P$	$P_1 \times \theta_1^{35} \times n_{P,1}^{35} =$ 0.5741*1*1	$P_2 \times \theta_2^{35} \times n_{P,2}^{35} =$ 0.3672*$\frac{k_{35}}{k_{35}+k_{37}}$*0	$P_3 \times \theta_3^{35} \times n_{P,3}^{35} =$ 0.0587*0*0
	$P_1 \times \theta_1^{37} \times n_{P,1}^{35} =$ 0.5741*0*1	$P_2 \times \theta_2^{37} \times n_{P,2}^{35} =$ 0.3672*$\frac{k_{37}}{k_{35}+k_{37}}$*1	$P_3 \times \theta_3^{37} \times n_{P,3}^{35} =$ 0.0587*1*0
$^{37}Cl_P$	$P_1 \times \theta_1^{35} \times n_{P,1}^{37} =$ 0.5741*1*0	$P_2 \times \theta_2^{35} \times n_{P,2}^{37} =$ 0.3672*$\frac{k_{35}}{k_{35}+k_{37}}$*1	$P_3 \times \theta_3^{35} \times n_{P,3}^{37} =$ 0.0587*0*1
	$P_1 \times \theta_1^{37} \times n_{P,1}^{37} =$ 0.5741*0*0	$P_2 \times \theta_2^{37} \times n_{P,2}^{37} =$ 0.3672*$\frac{k_{37}}{k_{35}+k_{37}}$*0	$P_3 \times \theta_3^{37} \times n_{P,3}^{37} =$ 0.0587*1*1

[a] $\Pi_R={}^{37}R_{std}/({}^{37}R_{std}+1)=0.2423$.

Using the parameters in Table S1, we have,

$$\frac{{}^{37}Cl_P}{{}^{35}Cl_P} = \frac{P_1 \times \theta_1^{35} \times n_{P,1}^{37} + P_2 \times \theta_2^{35} \times n_{P,2}^{37} + P_3 \times \theta_3^{35} \times n_{P,3}^{37} + P_1 \times \theta_1^{37} \times n_{P,1}^{37} + P_2 \times \theta_2^{37} \times n_{P,2}^{37} + P_3 \times \theta_3^{37} \times n_{P,3}^{37}}{P_1 \times \theta_1^{35} \times n_{P,1}^{35} + P_2 \times \theta_2^{35} \times n_{P,2}^{35} + P_3 \times \theta_3^{35} \times n_{P,3}^{35} + P_1 \times \theta_1^{37} \times n_{P,1}^{35} + P_2 \times \theta_2^{37} \times n_{P,2}^{35} + P_3 \times \theta_3^{37} \times n_{P,3}^{35}}$$

$$= \frac{0.3672 \times \frac{k_{35}}{k_{35}+k_{37}} + 0.0587}{0.5741 + 0.3672 \times \frac{k_{37}}{k_{35}+k_{37}}} = \frac{0.4259k_{35} + 0.0587k_{37}}{0.5741k_{35} + 0.9413k_{37}} = \frac{0.4259KIE_{Cl} + 0.0587}{0.5741KIE_{Cl} + 0.9413}$$

2 Experimental Method and Results

2.1 Experimental Method

In our crossed-beam 3D-VMI apparatus, the product ion detector consists of a set of multichannel plates and a Delay-Line-Detector (DLD 80, commercially available from Roentdek). The procedure to obtain the 3D signals can be found elsewhere[19-24]. In the present experiments, a supersonic *iso*-$C_2H_2Cl_2$ beam from a nozzle (with a 30-μm aperture) was collimated with a 0.51-mm skimmer at the 23-mm downstream of the nozzle orifice and flies along y' axis in the laboratory coordinate. The *iso*-$C_2H_2Cl_2$ reagents were randomly oriented with respect to the pulsed Ar^+ beam. The Ar^+ ions were produced by the 30 eV-electron impacts, in which the intensity ratio of $Ar^+(^2P_{3/2})$: $Ar^+(^2P_{1/2})$ was about 2 :1. High-purity (99.99%) samples (Ar and *iso*-$C_2H_2Cl_2$) were available commercially and used without further purifications, in which the stable isotopes ^{13}C, ^{38}Ar, and ^{36}Ar were not considered in this study due to their much lower abundances or concentrations (^{12}C : $^{13}C \approx 90$: 1; ^{40}Ar: ^{38}Ar: $^{36}Ar \approx 1581$: 5: 1). The kinetic energy (or velocity) and its spread of the reactants were calibrated prior to the experiments. The relatively large kinetic energy spread of Ar^+ ions ($\Delta E/E \sim 8\%$) was the main factor which impeded further improvement of the velocity resolution of the ion image. Meanwhile, the energy difference between $Ar^+(^2P_{3/2})$ and $Ar^+(^2P_{1/2})$ was considered under the present energy resolution. The product ions and scattered Ar^+ were pushed out by applying a voltage pulse on the repeller of the VMI lenses. A Newton sphere of the product ions gradually grew up (along z' axis) and was finally detected at the end of the VMI system, while the Ar^+ ions as the reaction residuals were pushed outside and very few could reach the detector. During the DCE experiments, the reaction chamber was evacuated under a steady vacuum condition of 5.3×10^{-7} Torr and the reactions happen in the field-free region. The working frequency was 10 kHz, and dozens of hours were spent to record the ion signals at each collision energy.

2.2 Procedure of Data Analysis

The energetic thresholds (E_{th}) of the following DCE reactions are estimated with the thermodynamics data[23-25] and

references cited therein,

$$Ar^+ + iso\text{-}C_2H_2Cl_2 \rightarrow Ar + H + C_2HCl_2^+ \ (E_{th} = -2.36eV),$$

$$Ar^+ + iso\text{-}C_2H_2Cl_2 \rightarrow Ar + Cl + C_2H_2Cl^+ \ (E_{th} = -3.70eV),$$

$$Ar^+ + iso\text{-}C_2H_2Cl_2 \rightarrow Ar + H + Cl + C_2HCl^+ \ (E_{th} = 0.67eV) \text{ and}$$

$$Ar^+ + iso\text{-}C_2H_2Cl_2 \rightarrow Ar + HCl + C_2HCl^+ \ (E_{th} = -3.81eV).$$

Above E_{th} values are obtained only for the reagent $Ar^+(^2P_{3/2})$, because its higher-state $Ar^+(^2P_{1/2})$ has an intensity about half of the $Ar^+(^2P_{3/2})$ ions in our electron-impact ion source. Due to the translational-to-internal energy transformation, all of above reactions are allowed in energetics in the collision energy range investigated here. Note that the appearance energy of $C_2H_2Cl^+$ in the dissociative photoionization was observed at 11.88 eV and corresponds to an E_{th} value about -3.88 eV for the DCE reaction with $Ar^+(^2P_{3/2})$.

Table S2 Intensity ratios of the isotopic ions and branching ratios of different ionic yields.

$E_{c.m.}$[a)]		$C_2H^{35}Cl_2^+$: $C_2H^{35}Cl^{37}Cl^+$	$C_2H_2{}^{35}Cl^+$: $C_2H_2{}^{37}Cl^+$	$C_2H^{35}Cl^+$: $C_2H^{37}Cl^+$
2.58eV	Intensity Ratio	1.29±0.39 : 1	2.94±0.20 : 1	0.29±0.04 : 1
	Branching Ratio[b)]	1.7±0.3%(dehydronation)	62.9±2.5%(dechlorination)	33.6±2.0%(dehydrochlorination)
3.95eV	Intensity Ratio	1.32±0.34 : 1	3.88±0.34 : 1	0.31±0.04 : 1
	Branching Ratio[b)]	1.8±0.3%(dehydronation)	63.5±2.6%(dechlorination)	33.8±2.1%(dehydrochlorination)
4.67eV	Intensity Ratio	1.48±0.26 : 1	3.41±0.24 : 1	0.30±0.04 : 1
	Branching Ratio[b)]	1.6±0.2%(dehydronation)	61.4±2.2%(dechlorination)	35.1±1.8%(dehydrochlorination)
8.90eV	Intensity Ratio	1.33±0.32 : 1	3.40±0.34 : 1	0.27±0.05 : 1
	Branching Ratio[b)]	2.6±0.4%(dehydronation)	58.9±3.0%(dechlorination)	36.0±2.6%(dehydrochlorination)

[a)]Collision energy is given only for the most abundant isotopic reagent $C_2H_2{}^{35}Cl_2$.
[b)]Considering the production of the parent cation, but its percentages are not presented in Table.

We fitted the TOF mass spectra with the Gaussian-profile peaks. As shown in Fig. 1b, the peak widths of the $^{35,37}Cl$-species of a certain type of yields were same, but the peak width of $C_2H^{37}Cl^+$ was always larger than that of $C_2H^{35}Cl^+$. Correspondingly, in the latter case, the velocity images in Figs. 2e-2f showed that the distributions of $C_2H^{37}Cl^+$ were diffuser than those of $C_2H^{35}Cl^+$. In slicing the images, a proper thickness (ca. 60 ns) at the Newton

aspheric equator (around the peak center in the TOF mass spectra) is used to avoid the interference of two different ionic yields.

In the dissociative photoionization, $C_2H_2Cl^+$ and $C_2H_2^+$ ions, as well as the parent cation, are the predominant fragments[26]. However, C_2HCl^+, instead of $C_2H_2^+$, is another main ionic yield in the DCE reactions. As shown in Fig. 1b, four types of ionic yields (the ^{35,37}Cl-isotopic species) are observed. The parent cation, $C_2H_2{}^{37}Cl_2^+$, is not presented in Fig. 1b, due to its much less abundance (about 6% of the reagent) in nature. Note that the $C_2H_2{}^{35}Cl^+$ and $C_2H^{35}Cl^+$ ions can be produced either from *iso*-$C_2H_2{}^{35}Cl_2$ or *iso*-$C_2H_2{}^{35}Cl^{37}Cl$, while their ^{37}Cl-speices are produced either from *iso*-$C_2H_2{}^{35}Cl^{37}Cl$ or *iso*-$C_2H_2{}^{37}Cl_2$. Therefore, the intramolecular competition between C-^{35}Cl and C-^{37}Cl bond cleavages plays an important role in the Cl-isotope effects.

The collision energies are changed for the different *iso*-$C_2H_2Cl_2$ isotopologues. For example, the $E_{c.m.}$ values of 2.58, 3.95, 4.67 and 8.90 eV for $C_2H_2{}^{35}Cl_2$ correspond to 2.60, 3.98, 4.67 and 8.95 eV for $C_2H_2{}^{35}Cl^{37}Cl$, respectively. The dehydronated ions $C_2H^{35}Cl_2^+$ and $C_2H^{35}Cl^{37}Cl^+$ are produced from $C_2H_2{}^{35}Cl_2$ and $C_2H_2{}^{35}Cl^{37}Cl$, respectively. Their velocity images in Fig. S1 indicate the most ions have the velocities close to that of the reagent molecule, implying a fast dehydronation process after the long-distance (or large impact-parameter) energy-resonant charge exchange between Ar^+ and *iso*-$C_2H_2Cl_2$. With reference to the photoelectron spectrum[26], the energy-resonant charge exchange results in the ro-vibrational states around $\tilde{F}$ state of *iso*-$C_2H_2Cl_2^+$. In the DCE reaction, only few of those *iso*-$C_2H_2Cl_2^+$ ions decay through the dehydronation, while the most of them prefer the dechlorination and dehydrochlorination. The latter can be witnessed with the strong signals of $C_2H_2Cl^+$ and C_2HCl^+ in Fig. 1b. All processes should start from the ro-vibrational states around $\tilde{F}$ state of *iso*-$C_2H_2Cl_2^+$ and decay nonadiabatically to the ground state $\tilde{X}$. Another point deserving attention is that the dehydronation can quickly cool

down the residual cation, because the most energy after the C-H bond cleavage could be taken away by the leaving atom H. According to this dynamic picture, we conclude that the dehydrochlorination observed in the experiment cannot be a sequential process, namely, without possibilities of the dehydronation-dechlorination cascade.

The KIE indicates the isotope effect of overall reaction, but does not show any information about the dependences on the product's velocity (or momentum) distribution. In Fig. 2 (also Fig. S1), the velocity images were depicted in their respective intensity scales, which helps readers to grasp the details therein. Fig. 3 shows the velocity (u_x) dependences of the $\delta^{37}Cl$ values of $C_2H_2Cl^+$ and C_2HCl^+ yields at the lowest collision energy. To the best of our knowledge, this is the first time that the distinctly different dynamic isotope effects are observed by the isotope-resolved VMI measurements.

3 AIMD Simulations

The entrance of the DCE reaction with Ar^+ usually lies at the energy level higher than that of the system consisting of Ar and the molecular cation, due the lower ionization threshold of the target [lower than the ionization potential of 15.579 eV for $Ar^+(^2P_{3/2})$]. The charge transfer from Ar^+ is very fast (in few femtosecond or less), particularly in an energy-resonant process. In this work, the on-the-fly trajectories for the system (Ar…*iso*-$C_2H_2Cl_2^+$) mimic the dynamic processes after the instant charge transfer. Moreover, we only considered the head-on collisions with *iso*-$C_2H_2Cl_2$ in which the molecular orientation, i.e., the dichloride group pointing to Ar^+, was preferable because of the large dipole moment of *iso*-$C_2H_2Cl_2$.

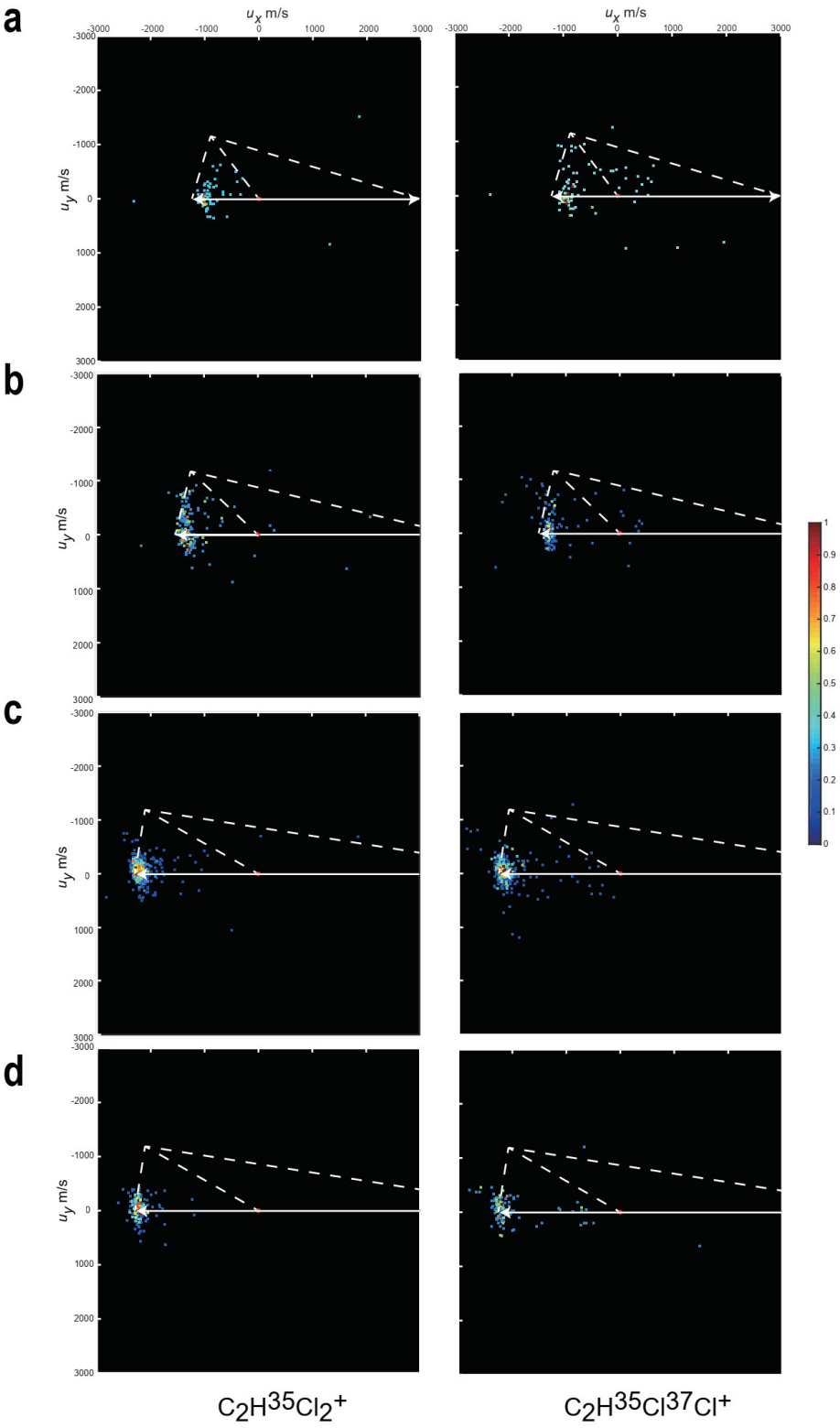

Fig. S1 Time-sliced velocity images of the isotopic products of $C_2HCl_2^+$. In the left panels, the collision energies in the center-of-mass (c.m.) coordinate are 2.58 (**a**), 3.95 (**b**), 4.67 (**c**) and 8.90 (**d**) eV for the most abundant isotopic reagent $C_2H_2{}^{35}Cl_2$, while in the right panels they are 2.60 (**a**), 3.98 (**b**), 4.70 (**c**) and 8.95 (**d**) eV for the $C_2H_2{}^{35}Cl^{37}Cl$. The ion intensities in each image are normalized independently. The notations of the velocities shown with broken and solid white lines can be found in the caption of Figure 2.

At the moment of the instant charge transfer from Ar^+ to *iso*-$C_2H_2Cl_2$, the equilibrium geometry of the neutral is maintained for the initial *iso*-$C_2H_2Cl_2^+$. This vertical-ionization alike process can be described with the Marcus long-distance charge transfer model, i.e., the Franck-Condon weighted density of states should be considered. Therefore, the first step of the trajectory simulations starts from *iso*-$C_2H_2Cl_2^+$ within the neutral arrangement, and the vibrations of υ_3, υ_4 and their combinational $\upsilon_3+\upsilon_4$ and $2\upsilon_3+\upsilon_4$ modes are selectively activated due to their large Franck-Condon factors observed with a high-resolution photoelectron spectroscopy[26]. These initial nuclear motions can be transferred to other motions by the collision.

The collision trajectories started from the intermolecular distance (Ar …*iso*-$C_2H_2Cl_2^+$) of 6Å. At the first step, the ionization potential difference 5.753 eV between $Ar^+(^2P_{3/2})$ and *iso*-$C_2H_2Cl_2^+$ (ref. 26) was put into the internal motions of *iso*-$C_2H_2Cl_2^+(X^2B_1)$. The collision energy $E_{c.m.}$ =2.60 eV was set up as the translational motion of Ar with respect to *iso*-$C_2H_2{}^{35}Cl^{37}Cl^+$. Meanwhile, the initial rotational temperature about 30 K was considered due to the retarding or cooling effect arising from the strong charge-dipole attraction. The Born-Oppenheimer MD simulations (with a step about 0.5 fs) were performed at the M06-2X/6-31+G(d,p) level of theory. Totally, we obtained 1233 trajectories in which 850 ones showed the molecular fragmentations. All calculations and simulations were performed with the suit program Gaussian 09 (ref. 27).

$C_2H_2Cl^+$, as the DCE yield, is preferred much more than C_2HCl^+, which is in qualitative agreement with the experimental results (see Fig. 1b). In the minor reaction pathways (labelled with '**others**' in Fig. S2), very few trajectories lead to $C_2H_2^+$ + 2Cl fragments, while it was found as the dominant channel of the dissociative photoionization at the photon energy > 16.5 eV (ref. 23). Meanwhile, the double-dehydronation processes (-2H and

–H_2) are observed. Additionally, we also find the isomerization from *iso*- to *cis*-$C_2H_2Cl_2^+$ in the non-fragmentation processes, which was proposed previously[25,26]. The times of the HCl formation are summarized in Fig. S3. They are classified into two types: the fast (denoted as case *a*) and slow (case *b*) ones.

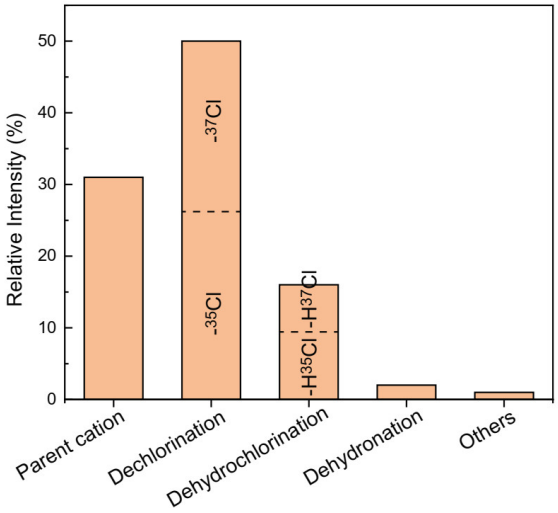

Fig. S2 Statistical data of the trajectories leading to molecular fragmentations. The simulations are performed at the collision energy 2.60 eV for *iso*-$C_2H_2{}^{35}Cl^{37}Cl$.

In Fig. 2, we find that the backward-scattered $C_2H_2Cl^+$ and C_2HCl^+ yields (Figs. 2a and 2e) turn to be distributed in the forward direction (Figs. 2d and 2e) with the increase of collision energy. As discussed in the text, the predissociative parent cation can fly forward in the large impact-parameter or peripheral collision and then the large daughter fragment $C_2H_2Cl^+$ or C_2HCl^+ would be produced in the forward direction. Therefore, we can deduce such a dynamic process for the $C_2H^{37}Cl^+$ yields adjacent to the center of mass (Fig. 2h): at the high collision energy (8.95 eV), the impact parameter of the DCE reaction would be a little larger than that illustrated in Fig. 4b, thus, the predissociative $C_2H_2{}^{35}Cl^{37}Cl^+$ could fly forward after a side-on (instead of head-on) charge transfer. With the increase of the impact parameter, the translational-to-internal energy transfer becomes unfavorable, thus the possibility of the DCE reaction leading to $H^{35}Cl$ plus $C_2H^{37}Cl^+$ is lower.

Here we must address the limitations of the present simulations: (i) Although the relative possibilities of dechlorination, dehydrochlorination, dehydronation, and others shown in Fig. S2 are generally in agreement with the relative intensities of the ionic yields ($C_2H_2Cl^+$, C_2HCl^+, $C_2HCl_2^+$). The charge-exchange-only process, i.e., the parent cation, predicted in Fig. S2, shows a relatively high contribution, which is contrary to the observation exhibited in Fig. 1b. This distinct difference indicates that the Marcus charge transfer model (i.e., the Franck-Condon weighted density of states) could be invalid[23]. (ii) Different impact parameters with their respective weighing factors should be considered in the large or small impact-parameter collisions. (iii) As mentioned in the main text, the pathway competitions among the charge-transfer-only, dechlorination, dehydrochlorination, dehydronation, and others that happen in the large or small impact-parameter collision are also essential to understand the Cl-isotope effect. In Fig. S2, one may find that the dehydrochlorination $-H^{35}Cl$ is more favorable than the $-H^{37}Cl$, which is partially in agreement with the results shown in Fig. 1c. The $\delta^{37}Cl$ values of the backward-scattered yields cannot be derived from the simulations, because we do not know the relative intensities or numbers of the rebounded $C_2H_2Cl_2^+$ isotopologues (due to the small impact-parameter collision). We cannot make any quantitative analyses of the present simulation results. Sophisticated simulations are highly demanded, but they are still challenging both in theory and computational capability.

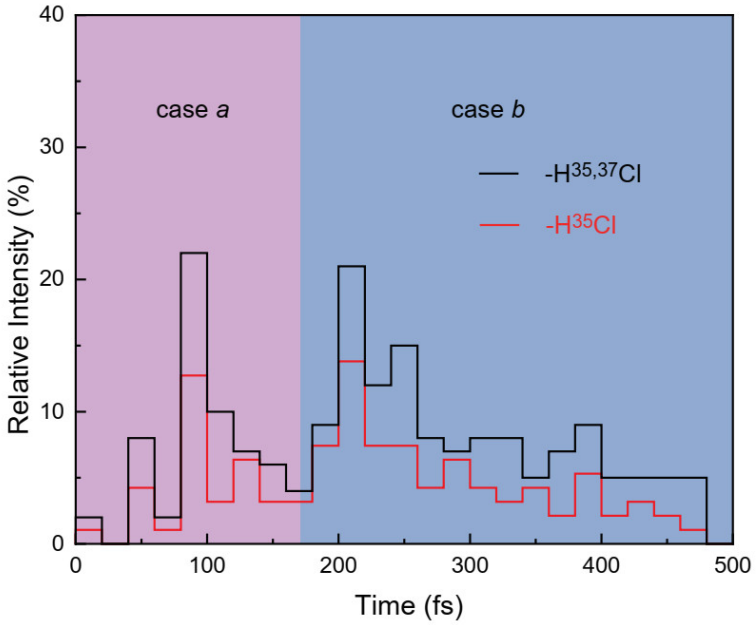

Fig. S3 Statistical data of the HCl formations. The simulations are performed at the collision energy 2.60 eV for *iso*-$C_2H_2{}^{35}Cl^{37}Cl$. The dynamic processes are classified into the fast (case *a*) and slow (case *b*) ones.

Reference

27. M. J. Frisch, G. W. Trucks, H. B. Schlegel, G. E. Scuseria, M. A. Robb, J. R. Cheeseman, G. Scalmani, V. Barone, B. Mennucci, G. A. Petersson, H. Nakatsuji, M. Caricato, X. Li, H. P. Hratchian, A. F. Izmaylov, J. Bloino, G. Zheng, J. L. Sonnenberg, M. Hada, M. Ehara, K. Toyota, R. Fukuda, J. Hasegawa, M. Ishida, T. Nakajima, Y. Honda, O. Kitao, H. Nakai, T. Vreven, J. A. Montgomery, Jr., J. E. Peralta, F. Ogliaro, M. Bearpark, J. J. Heyd, E. Brothers, K. N. Kudin, V. N. Staroverov, R. Kobayashi, J. Normand, K. Raghavachari, A. Rendell, J. C. Burant, S. S. Iyengar, J. Tomasi, M. Cossi, N. Rega, J. M. Millam, M. Klene, J. E. Knox, J. B. Cross, V. Bakken, C. Adamo, J. Jaramillo, R. Gomperts, R. E. Stratmann, O. Yazyev, A. J. Austin, R. Cammi, C. Pomelli, J. W. Ochterski, R. L. Martin, K. Morokuma, V. G. Zakrzewski, G. A. Voth, P. Salvador, J. J. Dannenberg, S. Dapprich, A. D. Daniels, Ö. Farkas, J. B. Foresman, J. V. Ortiz, J. Cioslowski, and D. J. Fox, *Gaussian 09* (Gaussian, Inc., Wallingford CT, 2009).

4 Appendixes

Movie S1 (movie S1.mp4) and Movie S2 (movie S2.mp4)

The H-scrambling (Movie S1, case *a*) and roaming (Movie S2, case *b*) can be clearly observed, and the subsequent ^{35}Cl-abstarction is preferred in both of these two cases. Two segments of the dehydrochlorination movies are selected and cartooned in Fig. 4b.